Current models of the observable consequences of cosmic reionization and their detectability

Iliev, I T ; Mellema, G ; Pen, U L ; Bond, J R ; Shapiro, P R

Abstract: A number of large current experiments aim to detect the signatures of the cosmic reionization at redshifts z > 6. Their success depends crucially on understanding the character of the reionization process and its observable consequences and designing the best strategies to use. We use large-scale simulations of cosmic reionization to evaluate the reionization signatures at redshifted 21-cm and small-scale cosmic microwave background (CMB) anisotropies in the best current model for the background universe, with fundamental cosmological parameters given by Wilkinson Microwave Anisotropy Probe three-year results. We find that the optimal frequency range for observing the 'global step' of the 21-cm emission is 120–150 MHz, while statistical studies should aim at 140–160 MHz, observable by GMRT. Some strongly non-Gaussian brightness features should be detectable at frequencies up to 190 MHz. In terms of sensitivity-signal trade-off relatively low resolutions, corresponding to beams of at least a few arcminutes, are preferable. The CMB anisotropy signal from the kinetic Sunyaev–Zel'dovich effect from reionized patches peaks at tens of K at arcminute scales and has an rms of 1 K, and should be observable by the Atacama Cosmology Telescope and the South Pole Telescope. We discuss the various observational issues and the uncertainties involved, mostly related to the poorly known reionization parameters and, to a lesser extend, to the uncertainties in the background cosmology.

DOI: https://doi.org/10.1111/j.1365-2966.2007.12629.x

Mon. Not. R. Astron. Soc. **000**, 1 (2006) Printed 4 February 2008 (MN LATEX style file v2.2)

Reionization observables after WMAP 3-year results

Ilian T. Iliev[1⋆], Garrelt Mellema[2], Ue-Li Pen[1], J. Richard Bond[1], Paul R. Shapiro[3],

[1] *Canadian Institute for Theoretical Astrophysics, University of Toronto, 60 St. George Street, Toronto, ON M5S 3H8, Canada*
[2] *Stockholm Observatory, AlbaNova University Center, Stockholm University, SE-106 91 Stockholm, Sweden*
[3] *Department of Astronomy, University of Texas, Austin, TX 78712-1083, U.S.A.*

4 February 2008

ABSTRACT

We use large-scale simulations of cosmic reionization to study the effect of varying the fundamental cosmological parameters on the reionization signatures. We compare two cases, one based on the WMAP 3-year data (WMAP3) characterized by a low $\sigma_8 = 0.74$ and one motivated by the WMAP 1-year data (WMAP1) with a high $\sigma_8 = 0.9$; dwarf galaxy formation is delayed by about 30% in redshift in the low σ_8 case. Current cosmological parameter estimates synthesizing all of the available data indicate these two cases should bracket the full range of dwarf galaxy formation epochs relevant to reionization. In WMAP3 cosmology reionization is delayed, resulting in all 21-cm signatures moving to significantly higher frequencies. This should significantly facilitate the redshifted 21-cm observations compared to previous expectations, due to the diminishing foregrounds and the rising instrument sensitivities at higher frequencies. We find that for WMAP3 the best frequency range for observing the "global step" of the 21-cm emission is 120-150 MHz, while statistical studies should aim at 140-160 MHz, observable by GMRT. Some strongly-nongaussian brightness features are observable at frequencies up to ~ 190 MHz. In terms of sensitivity-signal trade-off relatively low resolutions, corresponding to beams of at least a few arcminutes, are preferable. The CMB anisotropies due to patchy reionization have similar shape, but lower amplitude by factor of a few for WMAP3 compared to WMAP1. The signal peaks at tens of μK at arcminute scales and has an *rms* of $\sim 1\mu$K and should be observable by Atacama Cosmology Telescope and South Pole Telescope in both σ_8 cases.

Key words: H II regions—high-redshift—galaxies: formation—intergalactic medium—cosmology: theory—radiative transfer— methods: numerical

1 INTRODUCTION

The Epoch of Reionization and the preceding Cosmic Dark Ages, from recombination at $z \sim 1100$ to $z \sim 6$ include the formation of the first nonlinear cosmological structures, first stars, QSO's and the emergence of the Cosmic Web as we know it today. Yet it still remains poorly understood. This is mostly due to the scarcity of direct observations, resulting in weak constraints on the theoretical models. However, this situation is set to improve markedly in the coming years, with the construction of a number of new observational facilities, particularly for detection of the redshifted 21-cm line of hydrogen[1], and the kinetic Sunyaev-Zel'dovich (kSZ) effect[2].

Simulations of that epoch, required in order to make reliable predictions for such observations, are difficult and computationally-intensive. Recently we presented for the first time a set of large-scale, high-resolution radiative transfer simulations of cosmic reionization (Iliev et al. 2006b; Mellema et al. 2006b; Iliev et al. 2006c). These simulations were the first ones which were sufficiently large to reliably capture the characteristic scales

⋆ e-mail: iliev@cita.utoronto.ca

[1] Giant Metrewave Radio Telescope (GMRT; `http://www.ncra.tifr.res.in`), Low Frequency Array (LOFAR; `http://www.lofar.org`), Mileura Widefield Array (MWA; `http://web.haystack.mit.edu/arrays/MWA`), Primeval Structure Telescope (PAST; `http://web.phys.cmu.edu/$\sim$past/`), and Square Kilometre Array (SKA; `http://www.skatelescope.org`).
[2] South Pole Telescope (SPT; `http://spt.uchicago.edu/spt`) and Atacama Cosmology Telescope (ACT; `http://www.physics.princeton.edu/act/`)

of the reionization process. This allowed us to derive the first realistic predictions for the reionization observables, in particular the different signatures in the redshifted 21-cm emission of neutral hydrogen (Mellema et al. 2006b) and the imprint of the ionized patches on small-scale CMB temperature anisotropies through the kinetic Sunyaev-Zel'dovich (kSZ) effect (Iliev et al. 2006e,d). We also proposed an approach to use the obtained 21-cm maps to derive the Thomson optical depth fluctuations due to reionization (Holder et al. 2006) and derived the CMB polarization signatures of patchy reionization (Dore et al. 2007). We studied the effects of varying ionizing source efficiencies and sub-grid gas clumping on these observed signals. All of these calculations except Dore et al. (2007) used a particular set of cosmological parameters, based on the best-fit first-year WMAP results. A natural question to ask is how robust are these results against a variation of the basic cosmological parameters. This is an especially important question now, after the three-year WMAP data resulted in a significant adjustment to those parameters. The formation of cosmological structures at high redshifts is particularly sensitive to changes in the normalization of the power spectrum, usually expressed in terms of σ_8, the linear *rms* amplitude at the (top hat) scale $8\,h^{-1}Mpc$, and to any tilt in the index of the primordial power spectrum, n_s. The first dependence is because the sources responsible for reionization reside in rare halos, whose abundance is exponentially sensitive to the overall fluctuation amplitude. The second dependence is because the ionizing emissivity is dominated by small galaxies, of the size of present-day dwarf galaxies, or even smaller (down to $M \gtrsim 10^8\,M_\odot$), thus even a modest tilt of the power spectrum slope could change the abundances of such halos by a large amount.

After the dramatic recent improvements in the estimation of the fundamental cosmological parameters and the advent of the precision cosmology the values of these parameters are much better known than they were even a few years ago. However, some considerable uncertainties still remain. Detailed and precise simulations of the Epoch of Reionization like the ones presented here are still quite computationally expensive, thus it is not yet practical to cover the full allowed parameter space. Instead we adopt a different approach, whereby we ran series of simulations with the background cosmology at each of the extremes of the currently allowed range, which should bracket the range of possible outcomes. Throughout this work we assume a flat ($\Omega_k = 0$) ΛCDM cosmology. The first set of simulations, which we published previously (Mellema et al. 2006b; Iliev et al. 2006e,d) were based on the WMAP first year results, $(\Omega_m, \Omega_\Lambda, \Omega_b, h, \sigma_8, n) = (0.27, 0.73, 0.044, 0.7, 0.9, 1)$ (Spergel et al. 2003), hereafter WMAP1. The second set of simulations is based on the WMAP 3-year results, which derived the parameters $(\Omega_m, \Omega_\Lambda, \Omega_b, h, \sigma_8, n) = (0.24, 0.76, 0.042, 0.73, 0.74, 0.95)$ (Spergel & et al. 2006), hereafter WMAP3. Here Ω_m, Ω_Λ, and Ω_b are the total matter, vacuum, and baryonic densities in units of the critical density, σ_8 is the *rms* density fluctuations extrapolated to the present on the scale of $8h^{-1}$Mpc according to the linear perturbation theory, and n is the index of the primordial power spectrum of density fluctuations. We note that other measurements of these parameters based on e.g. other CMB experiments, supernovae, large-scale structure, clusters, and Ly-α forest tend to give slightly different values, either on their own or in combination with the WMAP data (e.g. Spergel & et al. 2006; Seljak et al. 2006; Yao & et al. 2006). In particular, they tend to yield higher value of σ_8 than WMAP3 alone (but still well below the WMAP1 value), at $\sigma_8 \sim 0.8 - 0.85$. For example, recent results using all of the CMB data derives $\sigma_8 = 0.79$, while combining with the large-scale structure data yields $\sigma_8 = 0.81$ (Kuo & et al. 2006). Therefore, the WMAP1 and WMAP3 cosmologies above could be considered as two limiting cases bracketing the actual background cosmology. Until the constraints are improved further we consider this the best approach to evaluate the effects of the the background cosmology on the reionization observables.

The major difference between the two bracketing cosmologies we have run is the overall amplitude, expressed here in terms of σ_8, but the models also have slightly different spectral shapes, with the low σ_8 one having a red tilt, $n_s - 1 = 0.05$. We have previously shown (Alvarez et al. 2006; Iliev et al. 2006c) that these changes result in structure formation being delayed in the WMAP3 universe relative to the WMAP1 universe, so the epoch of reionization is shifted to lower redshifts. In particular, if source halos of a given mass are assumed to have released ionizing photons with the same efficiency in either case, then reionization for WMAP3 is predicted to have occurred at $(1+z)$-values which are roughly 1.3-1.4 times smaller than for WMAP1. The predicted electron-scattering optical depth of the IGM accumulated since the beginning of the EOR would have then been smaller for WMAP3 than for WMAP1 by a factor of $(1.3 - 1.4)^{3/2} \sim 1.5 - 1.7$, just as the observations of large-angle fluctuations in the CMB polarization require. This means that the ionizing efficiency per collapsed baryon required to make reionization early enough to explain the value of $\tau_{\rm es}$ reported for WMAP1 and WMAP3 are nearly the same.

This delay of reionization can be understood in terms of the density fluctuations at the scales relevant to reionization as follows. Let us denote the *rms* linear amplitudes on the top hat smoothing scales of $0.1\,h^{-1}$Mpc and $0.01\,h^{-1}$Mpc by $\sigma_{0.1}$ and $\sigma_{0.01}$, respectively. The top hat scale $0.1\,h^{-1}$Mpc corresponds to a mass $2.7 \times 10^8 h^{-1}\,M_\odot$ for the low σ_8 case, and $3.1 \times 10^8 h^{-1}\,M_\odot$ for the high σ_8 case, the slight difference being due to the differing Ω_m and h. Of course $0.01\,h^{-1}$Mpc corresponds to masses 3 orders of magnitude smaller, $2.7 \times 10^5 h^{-1}\,M_\odot$ and $3.1 \times 10^5 h^{-1}\,M_\odot$, for WMAP3 and WMAP1. Thus, $\sigma_{0.1}$ and $\sigma_{0.01}$ roughly correspond to the scales of the dwarf galaxies and minihaloes, respectively. The shape difference in the low and high σ_8 cases is encoded in the ratios $\sigma_{0.1}/\sigma_8$, 6.1 and 6.6, and $\sigma_{0.01}/\sigma_8$, 10.1 and 11.0, that is, not negligible but not that large relative to the 20% decrease in σ_8. A reasonable indication of when structure on scale R formed at high redshift is $1 + z_R \approx 1.3\sigma_R\Omega_m^{-0.23}$, where $[a/D(z)] \approx \Omega_m^{0.23}$ for $z \gg 1$. Here $D(z)$ is the linear growth factor from redshift z to the present. For the minihalo scale $R = 0.01\,h^{-1}$Mpc, $z_{0.01} \approx 12.5$ and 16.4, respectively. For the dwarf scale $z_{0.1} \approx 7.1$ and 9.4, respectively, in reasonable accord with the computed overlap redshifts from our inhomogeneous reionization simulations (Iliev et al. 2006c, and Table 1 below); the 50% reionization redshifts bracket the minihalo and dwarf structure formation redshifts. The uniform reionization Thompson depth τ to a reionization redshift z_{rei} is $\tau = 0.085[(1+z_{rei})/11]^{3/2}$ for the low σ_8 model and $\tau = 0.080[(1+z_{rei})/11]^{3/2}$ for the high σ_8 model. When the $z_{50\%}$ values are substituted, there is rough agreement with the $\tau_{\rm es}$ in Table 1. The scaling of the Thompson depth τ would be $(1+z_R)^{3/2}$, about 1.4, roughly consistent with the ≈ 1.3 ratio we determine, and with the results in Alvarez et al. (2006) and Iliev et al. (2006c).

This paper is organized as follows. In § 2 we briefly describe our simulations. In § 3 we present our predictions for the redshifted 21-cm signals and discuss their observability with current and planned radio arrays. In § 4 we evaluate the patchy kSZ signal and its observability with ACT and SPT telescopes. Our conclusions are summarized in § 5.

2 SIMULATIONS

Our simulations were performed using a combination of two very efficient computational tools, a cosmological particle-mesh code called PMFAST (Merz et al. 2005) for following the structure formation, whose outputs are then post-processed using our radiative transfer and non-equilibrium chemistry code called C^2-Ray (Mellema et al. 2006a). Our simulations, parameters and methodology were discussed in Iliev et al. (2006b); Mellema et al. (2006b) and Iliev et al. (2006c). Detailed tests of the radiative transfer method used here were presented in Mellema et al. (2006a) and Iliev et al. (2006a). The simulations considered in this work are summarized in Table 1, along with the basic characteristics of their reionization histories[3]. The parameter f_γ characterizes the emissivity of the ionizing sources - how many ionizing photons per gas atom in the (resolved) halos are produced and manage to escape from the host halo within ~ 20 Myr, which is the time between two consecutive density slices, equal to two radiative transfer timesteps. Both WMAP3 simulations use $f_\gamma = 250$, as this value yields final H II region overlap at $z_{\rm ov} \approx 6.5 - 7.5$ in agreement with the current observational constraints. The corresponding integrated Thomson scattering optical depths, $\tau_{\rm es}$ are also in agreement, within 1-σ of the WMAP3 derived value, $\tau_{\rm es} = 0.09 \pm 0.03$, although they are a bit lower than the central value. The corresponding WMAP1 simulations with the same ionizing source efficiencies yielded $\tau_{\rm es} = 0.098 - 0.130$, outside of the nominal 1-σ WMAP1-derived range $\tau_{\rm es} = 0.17 \pm 0.04$. As we have previously shown (Iliev et al. 2006c), the presence of low-mass ionizing sources [unresolved here, but resolved in the smaller-box simulations presented in Iliev et al. (2006c)] increases the total optical depth, and can easily bring it into agreement with any value within the WMAP3 (or WMAP1, respectively) 1-σ range. In the same previous work we showed that despite this potentially dramatic effect on the integrated Thomson optical depth, the presence of small sources has only modest effects on the large-scale geometry of reionization, because most of these smaller sources were strongly clustered and as a consequence become strongly suppressed during the later stages of reionization due to Jeans-mass filtering within the ionized regions.

3 21-CM EMISSION

The differential brightness temperature with respect to the CMB of the redshifted 21-cm emission is determined by the density of neutral hydrogen, $\rho_{\rm HI}$, and its spin temperature, $T_{\rm S}$. It is given by

$$\begin{aligned}\delta T_b &= \frac{T_{\rm S} - T_{\rm CMB}}{1+z}(1 - e^{-\tau}) \\ &\approx \frac{T_{\rm S} - T_{\rm CMB}}{1+z}\frac{3\lambda_0^3 A_{10} T_* n_{HI}(z)}{32\pi T_S H(z)} \\ &= 28.5\,{\rm mK}\left(\frac{1+z}{10}\right)^{1/2}(1+\delta)\left(\frac{\Omega_b}{0.042}\frac{h}{0.73}\right)\left(\frac{0.24}{\Omega_m}\right)^{1/2}\end{aligned} \quad (1)$$

(Field 1959), where z is the redshift, $T_{\rm CMB}$ is the temperature of the CMB radiation at that redshift, τ is the corresponding 21-cm optical depth, $\lambda_0 = 21.16$ cm is the rest-frame wavelength of the line, $A_{10} = 2.85 \times 10^{-15}\,{\rm s}^{-1}$ is the Einstein A-coefficient, $T_* = 0.068$ K corresponds to the energy difference between the two levels, $1 + \delta = n_{\rm HI}/\langle n_H \rangle$ is the mean number density of neutral hydrogen in units of the mean number density of hydrogen at redshift z,

$$\begin{aligned}\langle n_H \rangle(z) &= \frac{\Omega_b \rho_{\rm crit,0}}{\mu_H m_p}(1+z)^3 \\ &= 1.909 \times 10^{-7}{\rm cm}^{-3}\left(\frac{\Omega_{\rm b}}{0.042}\right)(1+{\rm z})^3,\end{aligned} \quad (2)$$

with $\mu_H = 1.32$ the corresponding mean molecular weight (assuming 32% He abundance by mass), and $H(z)$ is the redshift-dependent Hubble constant,

$$\begin{aligned}H(z) &= H_0[\Omega_{\rm m}(1+z)^3 + \Omega_{\rm k}(1+z)^2 + \Omega_\Lambda]^{1/2} \\ &= H_0 E(z) \approx H_0 \Omega_{\rm m}^{1/2}(1+z)^{3/2},\end{aligned} \quad (3)$$

where H_0 is its value at present, and the last approximation is valid for $z \gg 1$. Throughout this work we assume that all of the neutral IGM gas is Ly-α-pumped and sufficiently hot (due to e.g. a small amount of X-ray heating) above the CMB temperature and is thus seen in emission. These assumptions are generally well-justified, except possibly at the earliest times (see e.g. Furlanetto et al. 2006, and references therein).

Table 1. Simulation parameters and global reionization history results for our runs.

	WMAP3		WMAP1	
	f250	f250C	f250	f250C
mesh	203^3	203^3	203^3	203^3
box size [h^{-1}Mpc]	100	100	100	100
f_γ	250	250	250	250
$C_{\rm subgrid}$	1	$C(z)$	1	$C(z)$
$z_{50\%}$	8.9	8.3	11.7	11
$z_{\rm overlap}$	7.5	6.6	9.3	8.2
$\tau_{\rm es}$	0.082	0.076	0.109	0.098

3.1 The progress of reionization: global view

The images shown in Figure 1 show the progress of reionization as seen at 21-cm emission vs. the observed frequency for run f250. The technique we used to produce them was described in detail in Mellema et al. (2006b) and is similar to the usual technique for producing light-cone images. In short, it involves continuous interpolation between the single-redshift numerical outputs in frequency/redshift space. The slices are cut at an oblique angle so as to avoid repetition of the same structures along the same line-of-sight and include redshift-space distortions. The top image shows the decimal logarithm of the differential brightness temperature at the full resolution of the simulation data, approximately 0.25' in angle and 30 kHz in frequency. The general character of reionization is very similar to the one observed for WMAP1 cosmology parameters. The ionization starts from the highest density peaks, which is where the very first galaxies form. These high peaks are

[3] WMAP1 cases listed here were first presented in (Mellema et al. 2006b), with predictions of 21-cm background and kSZ effect from patchy reionization from those cases presented in Mellema et al. (2006b) and Iliev et al. (2006d), respectively.

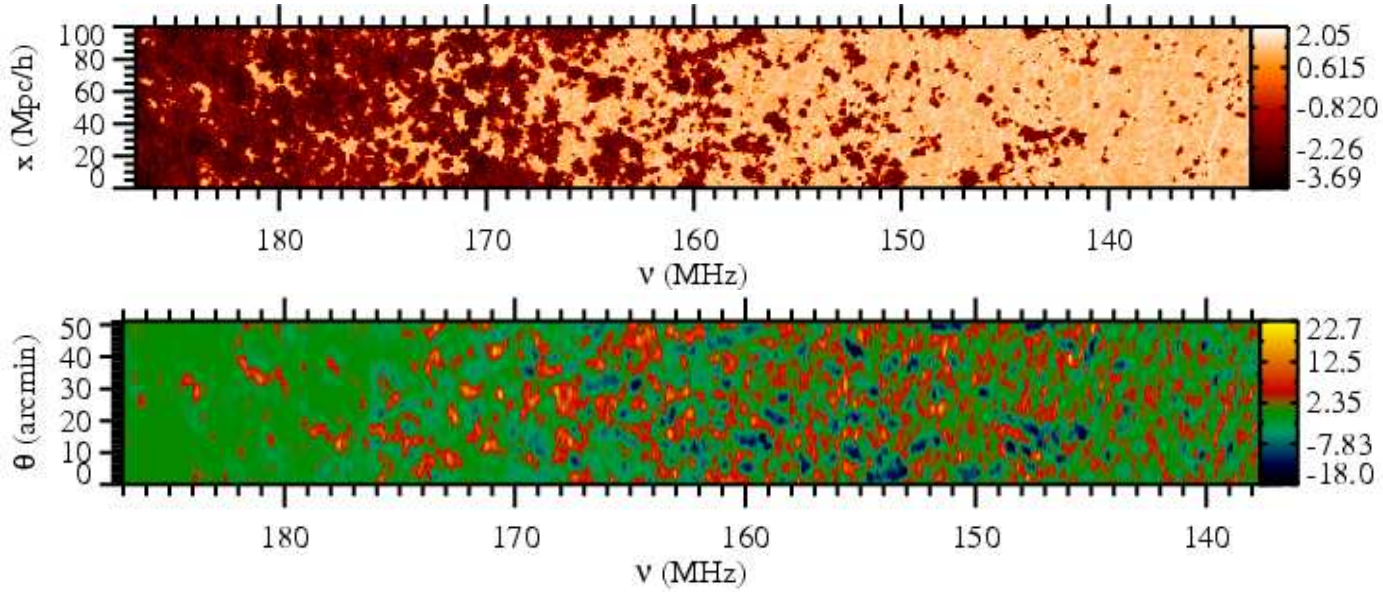

Figure 1. Position-redshift slices from the f250C simulation. These slices illustrate the large-scale geometry of reionization and the significant local variations in reionization history as seen at redshifted 21-cm line. Observationally they correspond to slices through an image-frequency volume. The top image shows the decimal log of the differential brightness temperature at the full grid resolution, while the bottom image shows the same data, but smoothed with a compensated Gaussian beam of 3' and (tophat) bandwidth of 0.2 MHz, roughly corresponding to the expected parameters for LOFAR. The spatial scale is given in comoving units (top) or (approximate) angle on the sky in arcminutes (bottom).

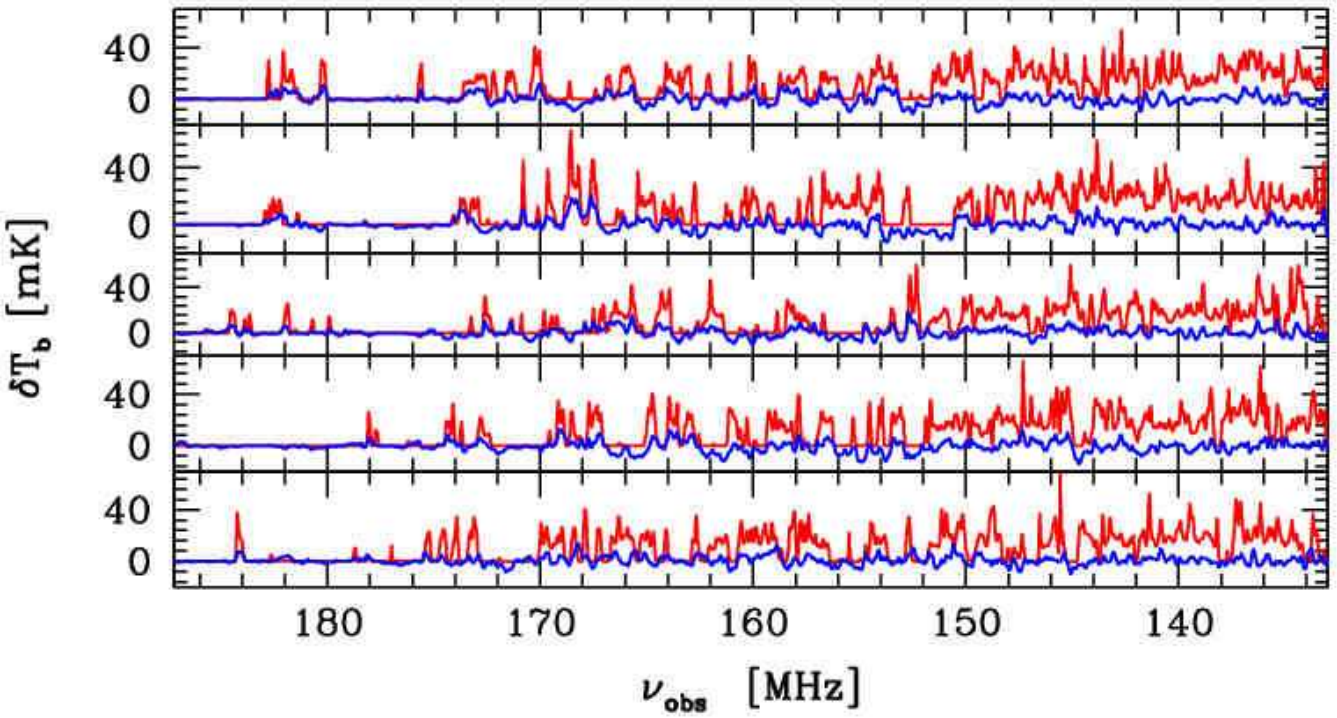

Figure 2. Sample line-of-sight 21-cm spectra obtained from our simulation data (simulation f250C). Shown are the full-resolution (red) and the beam- and frequency-smoothed spectra. (blue). For the latter we used a compensated Gaussian beam with a FWHM of $3'$ and a bandwidth of 0.2 MHz.

strongly clustered at high redshifts, which results in a quick local percolation of the ionized regions. As a result, by $z \sim 9$ ($\nu_{\rm obs} \sim 140$ MHz) already a few fairly large ionized regions form, each of size ~ 10 Mpc. These continue to grow and overlap until there is only one topologically-connected H II region in our computational volume, which for this particular simulation occurs at $z \sim 7$ ($\nu_{\rm obs} \sim 180$ MHz). However, even at this time quite large, tens of Mpc across, neutral regions still remain. They are gradually ionized as time goes on, but some of them persist until the very end of our simulation.

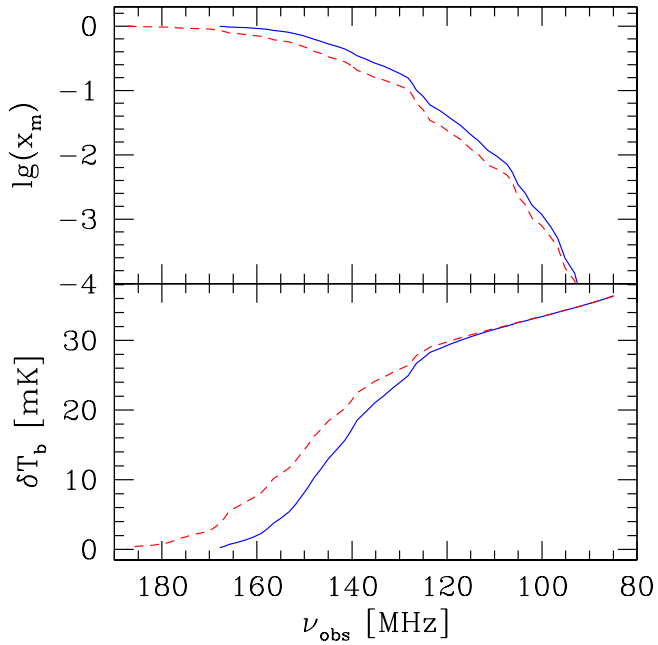

Figure 3. Evolution of the mean mass-weighted ionized fraction, x_m, (top), mean flux in μ Jy (assuming a circular beam with an angular diameter of 10') (middle) and the mean differential brightness temperature, δT_b, in mK vs. observed frequency for simulations f250 (solid, blue), and f250C (short-dashed, red).

The second image in Figure 1 shows the same data as the first, but as would be seen by a radio interferometer array assuming perfect foreground removal. To obtain it we smoothed the data with a compensated Gaussian beam with FWHM of 3' and bandwidth of 0.2 MHz, similar to the expected parameters for LOFAR. Unless otherwise stated, throughout this paper we use a compensated Gaussian beam. While it is not perfect match to the actual interferometer beam, it captures its essential properties. In particular, it has zero mean, and negative troughs at the side of the central peak (see e.g. Mellema et al. 2006b). As a result, ionized regions show as negative differential brightness temperature regions if they are surrounded by nearby neutral volumes. If an ionized (or neutral) region is much larger than the smoothing length, the resulting signal would be close to zero. A direct comparison between the two images shows that all the main structures clearly appear also in the smoothed image, indicating that LOFAR and other similar interferometers would have sufficient resolution to determine the large-scale reionization morphology to a reasonable accuracy throughout most of the reionization history. However, at the earliest stages of reionization some of the existing H II regions are barely seen, or not at all, since they are either merged with other nearby ionized regions, or simply smoothed away. This is due to the small sizes of these early H II regions, which puts most of them below the resolution. At frequencies higher than ~ 140 MHz the ionized bubbles become large enough to be above the smoothing scale and thus all major structures become visible. The Cosmic Dark Ages and the early stages of reionization might be still observable through other sources of 21-cm fluctuations not accounted for here. These include e.g. the 21-cm emission and absorption by cosmological minihaloes (Iliev et al. 2002; Furlanetto & Loeb 2002; Iliev et al. 2003), by shock-heated IGM (Furlanetto & Loeb 2004; Shapiro et al. 2006), or due to inhomogeneous early backgrounds in Ly-α (Chuzhoy et al. 2006) or X-rays (Pritchard & Furlanetto 2006).

The same data can be used for producing line-of-sight 21-cm emission spectra, at either full resolution or beam-smoothed. A few randomly-chosen samples of such spectra are shown in Figure 2. The beam- and bandwidth-smoothing leads to some loss of detail, e.g. some finer features blend together, but most large-scale fluctuation remain clearly visible. The typical peak amplitudes of the smoothed fluctuations are lower, but only moderately so. We would quantify this effect better in § 3.3. We note that there are bright and potentially observable features in the spectra even for $\nu_{\rm obs} > 180$ MHz, which is important for the planned observations since at such high frequencies both the foregrounds and the Radio Frequency Interference (RFI) are substantially lower, while at the same time the array sensitivities improve. We discuss these issues in more detail in § 3.5.

3.2 The mean background

In Figure 3 we show the evolution of the mean (i.e. averaged over a large volume) mass-weighted ionization fraction, x_m, and the mean differential brightness temperature as seen at the observer, $\overline{\delta T_b}(\nu_{\rm obs})$. As the universe steadily becomes ever more ionized, the mean 21-cm differential brightness temperature naturally decreases. However, non-trivial level of the signal (a few mK or more) persists until quite late, up to frequencies of 150-170 MHz. Similarly to our previous results which used the WMAP1 parameters, the "global step" from mostly-neutral to mostly-ionized medium (Shaver et al. 1999) turns out to be rather gradual, with the signal decreasing by $\sim$ 20 mK over 20-30 MHz (and somewhat more gradual for case f250C than for f250). Such an observation would be difficult, but still potentially possible (see Shaver et al. 1999, for more detailed discussion of the various observational issues). This brightness temperature behaviour suggests that the best frequency range for trying to observe the global step could be $\sim 120 - 150$ MHz, since there the signal decreases fastest.

The differential brightness temperature scales with the reionization redshift as $\delta T_b \propto (1+z)^{1/2}$. Thus, a delay of reionization from WMAP1 to WMAP3 model by 1.3 in redshift corresponds to an expected δT_b decrease by a factor of 1.14, roughly as found in our simulations.

3.3 The statistical measures

An alternative approach for detecting the progress of reionization would be to do it statistically, through detection of the fluctuations of the emission around its mean value. These fluctuations are due to a combination of the patchiness of reionization and variations of the underlying density field. In Figure 4 we show the *rms* of the 21-cm emission fluctuations derived from our simulations. The top panel shows the evolution of the differential brightness temperature *rms*, $\delta T_{\rm b,rms}$, for three choices for the beam size (in arcmin; using compensated Gaussian beam) and the bandwidth (in MHz), from top to bottom, $(\Delta\theta_{\rm beam}, \Delta\nu_{\rm bw}) = (0.1, 1)$ (roughly as expected for the SKA compact core), $(0.2, 3)$ (LOFAR) and $(0.4, 6)$ (GMRT, MWA). The middle panel shows the evolution of the corresponding fluxes, given by

$$\delta F(\nu_{\rm obs}) = \frac{2\nu_{\rm rec}^2}{c^2} k_B \delta T_b(\nu_{\rm obs}) \Delta\Omega, \qquad (4)$$

where $\Delta\Omega = \pi(\theta/2)^2$ is the 3D angle subtended by the beam for a circular beam with FWHM of $\theta_{\rm beam}$. On the bottom panel we

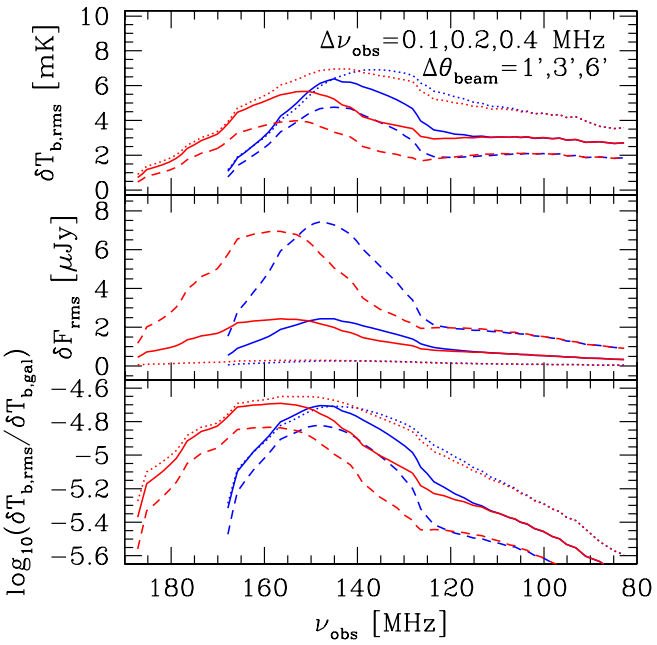

Figure 4. (a)(top) *rms* fluctuations of the differential brightness temperature, $\delta T_{\rm b,rms} \equiv \langle \delta T_b^2 \rangle^{1/2}$ vs. observed frequency, $\nu_{\rm obs}$ for f250 (blue) and f250C (red) for beam sizes and bandwidths $\Delta\theta_{\rm beam}, \Delta\nu_{\rm bw})$ =(1',0.1 MHz) (dotted), (3',0.2 MHz) (solid) and (6',0.4 MHz) (dashed); (b)(middle) Fluxes in μJy corresponding to the differential brightness temperature fluctuations in (a), same notation as in (a); and (c)(bottom) Ratio of $\delta T_{\rm b,rms}$ to the Galactic synchrotron foreground, assumed to be $\delta T_{\rm b,gal} = 300\,{\rm K}(\nu/150\,{\rm MHz})^{-2.6}$, same notation as in (a).

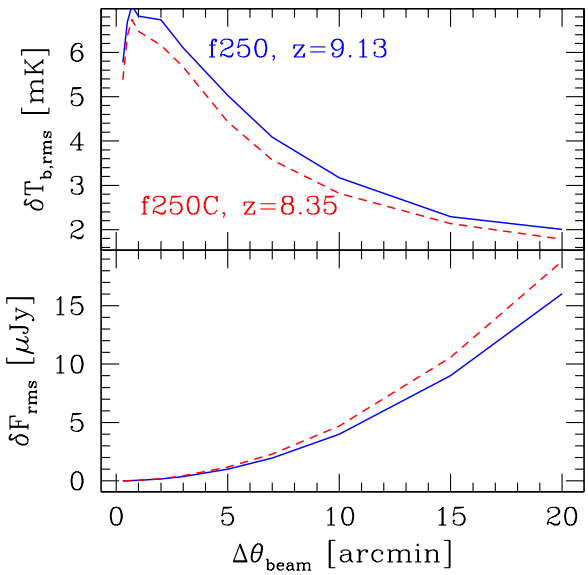

Figure 5. (a)(top) *rms* fluctuations of the differential brightness temperature, $\delta T_{\rm b,rms} \equiv \langle \delta T_b^2 \rangle^{1/2}$ vs. beam-size, $\delta\theta_{\rm beam}$ for f250 (solid, blue) and f250C (short-dashed, red) at redshifts close to the maximum of the fluctuations, as indicated. The bandwidth is changed in proportion to the beamsize. (b)(bottom) Flux fluctuations corresponding to the differential brightness temperature fluctuations in (a), same notation as in (a).

show the 21-cm signal as a fraction of the dominant foreground, the Galactic synchrotron emission. For the larger beams/bandwidths the $\delta T_{b,rms}$ peak is at $z \sim 8.8$ ($\nu_{\rm obs} \sim 145$ MHz) for f250 and at $z \sim 8.3$ ($\nu_{\rm obs} \sim 152 - 153$ MHz to for f250C, close to the time at which 50% of the mass is ionized, as was the case also for our WMAP1 results (Mellema et al. 2006b). However, for the higher resolution, with $1'$ beam, the peak of the fluctuations moves to noticeably earlier times/lower frequencies, and is at ~ 137 MHz ($x_m = 0.26$) for f250 and at ~ 143 MHz ($x_m = 0.26$) for f250C. This high-resolution case differs from the rest because the scales probed by such a small beam/bandwidth combination are generally below the characteristic bubble size. The exception is at early times, when ionized bubbles are still small on average, and thus match better the smaller beam-size, which is reflected in the fluctuation peak moving to earlier times.

Interestingly, the flux fluctuations peak somewhat later than the corresponding temperature fluctuations. In this case the position of the peak in redshift/frequency space is largely independent of the resolution employed, and is at $\sim 148-150$ MHz for f250 and at $\sim 155 - 157$ MHz for f250C. As the beam-size and bandwidth increase from 1' to 3' and then to 6', the temperature fluctuations decrease, albeit only by a modest amount. For example, the peak fluctuations for $(\Delta\theta_{\rm beam}, \Delta\nu_{\rm bw})$ =(6',0.4 MHz) are only a factor of ~ 2 lower (4 mK vs. 8 mK), while the corresponding flux increases by over an order of magnitude, indicating that it would be optimal to observe at relatively large scales, where we maximize the sensitivity without sacrificing much of the signal.

The 21-cm temperature fluctuations as fraction of the dominant foreground, the Galactic synchrotron (bottom panel) peak even later than the flux fluctuations. This is due to the broad peak of the 21-cm emission and the steep decline of this foreground at higher frequencies, which combine to push the peak to later times/higher frequencies, at $\nu_{\rm obs}$ up to 160-165 MHz. The signal is strongly dominated by the foregrounds at all times, but up to an order of magnitude could be gained for observations aimed close to the peak ratio, as opposed to earlier or later times.

This point is underscored further by Figure 5, where we plot the differential brightness temperature fluctuations and the corresponding fluxes vs. the instrument smoothing, as given by the beam size, with the bandwidth changed in proportion to the beam size. At small scales (below the typical ionized bubble size, a few arcmin or less) the temperature fluctuations are fairly large (> 6 mK) and dominated by Poisson fluctuations (e.g. a cell is either ionized or else is neutral). However, the corresponding flux is tiny, below 1 μJy. Around the typical bubble scale ($\sim 5 - 10'$) the fluctuations are slightly lower, at $\sim 3 - 4$ mK, but the flux grows strongly, as $\delta\theta^2_{\rm beam}$ and reaches $\sim 5\mu Jy$ at $\delta\theta_{\rm beam} = 10'$. At even larger angles/bandwidths the ionization fluctuations gradually start contributing ever less to the total and in the large-scale limit the temperature fluctuations just follow the underlying density fluctuations (multiplied by the mean differential brightness temperature). The flux curve gradually flattens and at some point there is little or nothing to be gained by a further increase of the observed sky patch since the gain in angle is canceled by the decrease of the temperature fluctuations. Thus, again there is a clear trade-off between the signal level and the array sensitivity. The optimal scale for observations would depend on the best sensitivity which could be achieved by a particular radio array. For compact arrays the optimal beam size is around 10-20', but could be lower than that for sensitive arrays with large collecting area like SKA.

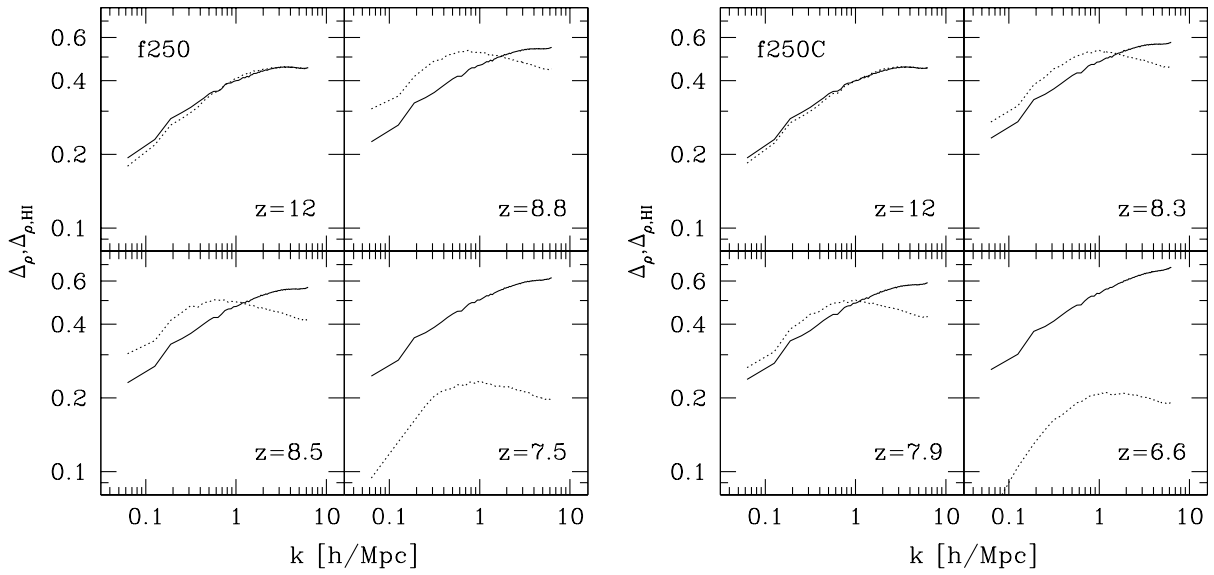

Figure 6. The variance, Δ of the 3D power spectra of the neutral gas density $\Delta_{\rho,HI}$ (dotted), and the total density Δ_ρ (solid), normalized to the total, for simulations f250 (left) and f250C (right). The redshifts are chosen as follows (in decreasing numerical order): early times ($z = 12$; $\overline{T_b} = 31.8$ mK for f250, $\overline{T_b} = 33.2$ mK for f250C), the redshift at which $\delta T_{\rm b,rms}$ peaks ($z = 8.8$, $\overline{T_b} = 13.1$ mK for f250, $z = 8.3$, $\overline{T_b} = 11.8$ mK for f250C), the redshift at which $\delta F_{\rm rms}$ peaks ($z = 8.5$, $\overline{T_b} = 8.9$ mK for f250; $z = 7.9$, $\overline{T_b} = 8.2$ mK for f250C), and the redshift of overlap ($\overline{T_b} = 0.3$ mK for f250; $\overline{T_b} = 0.2$ mK for f250C).

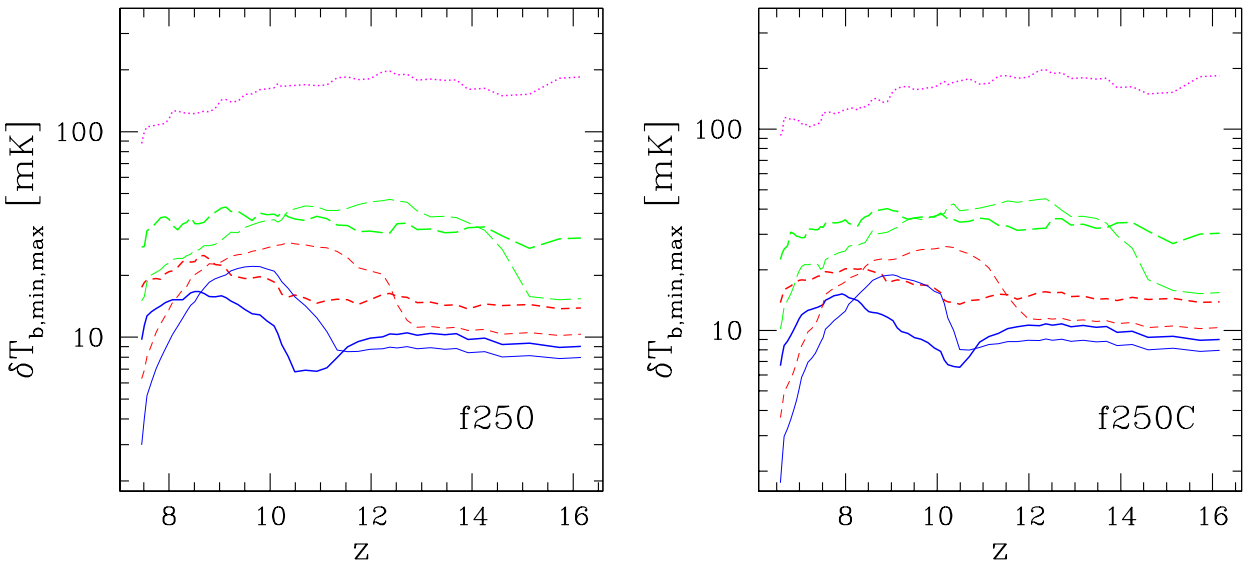

Figure 7. The brightest peak in the simulation box as a function of redshift, for simulations f250 (left), and f250C (right). Shown are the evolution of the maximum pixel value (thick lines) and minimum pixel value (thin; plotted is the absolute value since for compensated Gaussian beams the minimum values are negative) of the differential brightness temperature, δT_b vs. redshift z for several beam-sizes and bandwidths, as follows, $(\Delta\theta_{\rm beam}, \Delta\nu_{bw}) = (6, 0.4)$ (blue, solid), (3,0.2) (red, short-dashed), (1,0.1) (green, long-dashed) and the full resolution of our simulation (i.e. corresponding to single simulation cells; magenta, dotted), where the beam sizes are in arcminutes and the bandwidths are in MHz.

Finally, in Figure 6 we show the three-dimensional power spectra of the density and the neutral gas density fluctuations (to which the 21-cm signal is directly proportional) at several illustrative redshifts. Initially, the neutral density power largely tracks the one of the density field, since most of the gas is still neutral. At intermediate and late times the ionization fraction inhomogeneities introduce a peak around the characteristic scale of the ionized patches (which is $k \sim 1\,h\,Mpc^{-1}$ for f250C, and slightly lower for f250). Around the time when the fluctuations reach their peak the patchiness boosts the power on large scales by factor of ~ 2

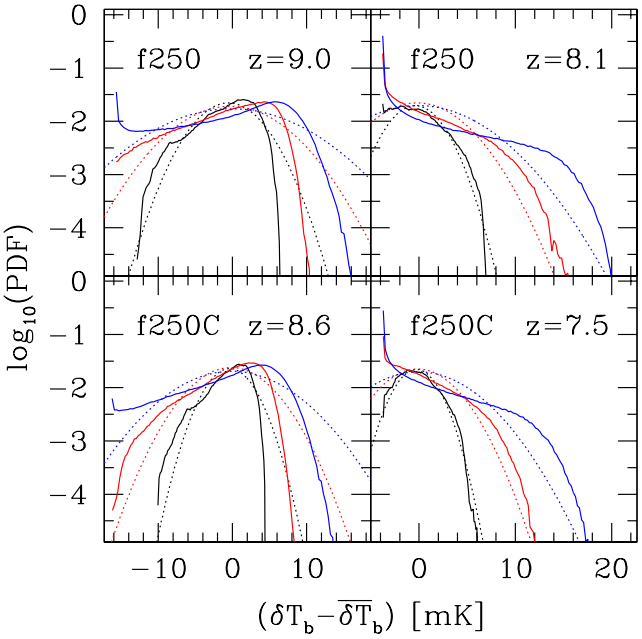

Figure 8. Non-Gaussianity of the 21-cm signal: PDF distribution of the 21-cm signal from simulation f250 for $z = 9.0$ (top left) and $z = 8.1$ (top right), and from simulation f250C for $z = 8.6$ (bottom left) and $z = 7.5$ (bottom right) for tophat beam. The PDF were derived for cubical regions of sizes $20\,h^{-1}Mpc$ (black solid), $10\,h^{-1}Mpc$ (red solid), and $5\,h^{-1}Mpc$ (blue solid). Also indicated are the Gaussian distributions with the same mean values and standard deviations (dotted, corresponding colours).

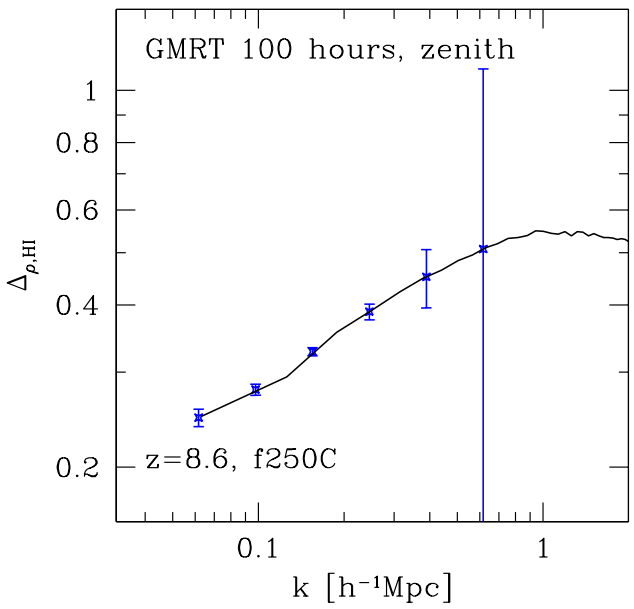

Figure 9. Observability of the 21-cm signal: the 3D power spectrum of the neutral hydrogen density, $\Delta_{\rho,HI}$, at redshift $z = 8.59$ ($\overline{T_b} = 16.3$ mK) with the forecast error bars for 100 hours observation with GMRT vs. wavenumber k. We assumed 15 MHz observing bandwidth (the full instantaneous bandwidth of GMRT), $T_{\rm sys} = 480$ K and assuming $T_S \gg T_{\rm CMB}$. The array configuration is assumed pointed to the zenith, but the sensitivity is only weakly dependent on the pointing.

(1.5) for f250 (f250C) compared to the density power spectrum. The signal largely disappears around the time of overlap, since little neutral hydrogen remains, but the power spectra still show the characteristic peak, at approximately the same scales.

3.4 Brightest features and their statistics

Some of the most visible redshifted 21-cm features would be the points of maximum departure of the signal from the mean. The magnitude of the signal is dependent on the level of smoothing and could evolve with redshift. In Figure 7 we plot the maximum (thick lines) and minimum (absolute value; thin lines) of the signal vs. redshift for both of our simulations using a compensated Gaussian beam. We show the results at three different levels of smoothing, as well as with no smoothing applied. In all cases the maxima/minima are roughly independent of redshift, within factor of ~ 2, but there are also some interesting and nontrivial features. For the case of no smoothing (i.e. at full grid resolution, $\sim 0.25'$, 30 kHz) the maximum amplitude is quite high, at $\sim 100-200$ mK. Naturally, the beam smoothing decreases the amplitude, to $\sim 20-30$ mK for $(\Delta\theta_{\rm beam}, \Delta\nu_{bw}) = (1', 0.1\,{\rm MHz})$, 10-20 mK for $(\Delta\theta_{\rm beam}, \Delta\nu_{bw}) = (3', 0.2\,{\rm MHz})$ and to 8-20 mK for $(\Delta\theta_{\rm beam}, \Delta\nu_{bw}) = (6', 0.4\,{\rm MHz})$. The introduction of subgrid clumping (f250 vs. f250C) results in only minor variations here. The absolute value of the minimum is similar to the one for the maximum in all cases, but the two still show some differences. For the larger beams/bandwidths the maxima peak around the time of 50% ionization by mass, while the absolute values of the minima peak noticeably earlier. This is readily understood based on the evolution of the typical ionized and neutral region sizes and the properties of the compensated Gaussian beam. Early-on the ionized regions are small and isolated, surrounded by large neutral patches, which yields deep negative minima at the positions of the ionized bubbles. At late times the H II regions grow large and the beam-smoothed signal inside them is close to zero. The positive maxima, on the other hand, are due to the densest neutral regions and are sampled by the central maximum of the beam, and thus reach their peak later.

The statistics of these emission peaks is also of considerable interest since it shows how common such features are and thus what patch of sky one needs to study for a detection. The PDFs of the 21-cm signal with respect to the mean signal are shown in Figure 8 for three different levels of smoothing (for tophat beam) and at two different evolution stages - close to 50% ionization (left panels) and at late times ($\sim 80\%$ ionization; right panels). All PDFs are considerably non-Gaussian, especially at late times and for smaller smoothing scale. In particular, for 5-10 Mpc smoothing scales there is an over-abundance of the brightest regions by up to an order of magnitude compared to the a Gaussian with the same mean and *rms*. At large scales ($20\,h^{-1}$ Mpc) and late times the PDF is very close to Gaussian.

3.5 Observability: redshifted 21-cm

There are several current or upcoming experiments which aim to detect the redshifted 21-cm signatures of reionization, including LOFAR, MWA, GMRT, PAST/21CMA and SKA. Not all details of the design and the instruments are yet known, particularly for SKA for which even the basic concept is not yet finalized. The only arrays currently in operation are GMRT and PAST/21CMA. Among

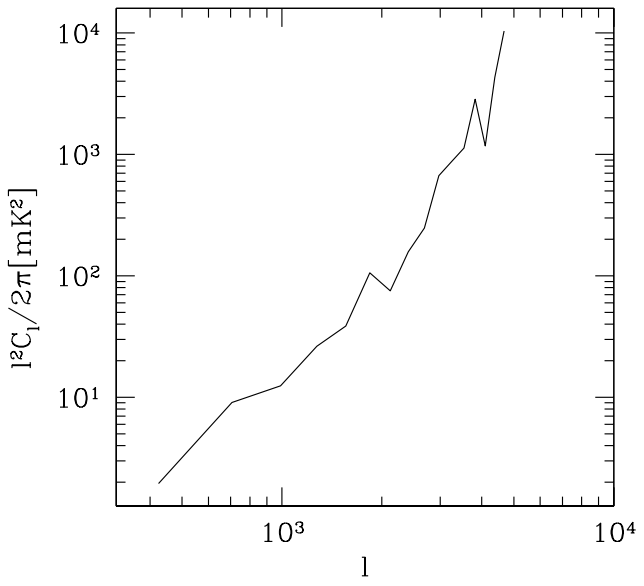

Figure 10. Observability of the 21-cm signal: angular power spectrum of thermal noise of GMRT for bandwidth of 15 MHz, 100 hours of integration, one single pointing.

these interferometers, GMRT and LOFAR have the largest collecting area, at $\sim 50,000\,\mathrm{m}^2$ for GMRT and (effective) $\sim 10^5\,\mathrm{m}^2$ for LOFAR at 110-200 MHz, and thus in principle they have the best sensitivity before the commissioning of SKA. However, the same two arrays also have significant interference problems to overcome from terrestrial sources of confusion. As an example, in Figure 9 we show our predicted 21-cm signal at $z = 8.6$ (case f250C) along with the GMRT sensitivity for 100 hours of integration. We assumed 15 MHz observing bandwidth (the full instantaneous bandwidth of the GMRT correlator, the frequency resolution is much better, of order kHz) and $T_{\rm sys} = 480$ K. The two small-k bins would probably not be observable due to foreground removal. The thermal noise of GMRT for bandwidth of 15 MHz, 100 hours of integration, and a single pointing is shown in Figure 10. The other two arrays, PAST/21CMA ($\sim 10^4\,\mathrm{m}^2$ effective area) and MWA ($\sim 7000\,\mathrm{m}^2$) are significantly smaller than LOFAR and GMRT, but are also more compact and would be in areas with very low interference, so could also be quite competitive.

Our results indicate that the 21-cm fluctuations in WMAP3 cosmology peak around $\nu_{\rm obs} = 130 - 170$ MHz (compared to 90-120 MHz for WMAP1 models), depending on the resolution and the detailed reionization parameters (ionizing source efficiencies and gas clumping). The corresponding 21-cm flux fluctuations, and the 21-cm temperature fluctuations as fraction of the foregrounds peak at even higher frequencies. These properties significantly facilitate the signal detection as compared to the WMAP1 cases, since at higher frequencies the detector sensitivities are dramatically better, while at the same time the foregrounds are lower, by roughly factor of $\sim (120/170)^{2.6} = 2.5$. The peak value of the differential brightness temperature fluctuations is $\sim 4 - 8$ mK, decreasing modestly with increasing beam and bandwidth. The corresponding fluxes are much more strongly dependent on the scale of observations, ranging from $< 1\mu$ Jy for 1' beam and 0.1 MHz bandwidth to $\sim 8\mu$ Jy for 6' beam and 0.4 MHz bandwidth. This clearly argues for relatively large beams, of at least a few arcmin, and for maximum collecting area concentrated in the compact core, in order to improve the sensitivity while not losing a significant fraction of the signal. For example, the expected sensitivity of LOFAR for 1 hour of integration time is $\sim 60\,\mu$Jy at $120 - 200$ MHz (and somewhat worse for the virtual core only), while its resolution is 3.5"-6" for the whole array and 3'-5' for the core. Thus, only the virtual core would be useful for EOR observations (although the extended part would be important for e.g. foreground subtraction). Upwards of 100 hours of integration time would be needed for detection, less if more antennae are placed in the virtual core.

The importance of aiming at the appropriate frequencies and length scales cannot be overstated. As we have shown, around the peak of the fluctuations the signal as fraction of the dominant foreground is up to an order of magnitude larger than it is off the peak. Utilizing an appropriate beam, i.e. one which is well-matched to the scale of the expected fluctuations and corresponding to sufficiently large flux level, given the available sensitivity, is also extremely important. Our results indicate that the best beam sizes are of at least a few arcminutes, and possibly much larger, of order 5-10' or more.

Another observational strategy, and one of the first to be proposed (Shaver et al. 1999) is to aim to detect the "global step" over the whole sky which reflects the transition from the fully-neutral universe before reionization to the fully-ionized one after. Since this is a global, all-sky signal it imposes essentially no requirements in terms of resolution. The sensitivity requirements are also relatively modest, since the flux corresponding to such a large area on the sky is very large. The main difficulty is the foreground subtraction. The global step we find is relatively gradual, ~ 20 mK over ~ 20 MHz. This would still be readily detectable in absence of foregrounds. How well the foregrounds could be subtracted would depend strongly on their properties, and in particular how fast and by how much the local slope of the power law describing it changes. If the foregrounds are well-fit by a single power law over the relevant frequencies, then there is a good chance to detect the global transition signal, see Shaver et al. (1999) for more detailed discussion.

An important reionization signature to look for is the one due to individual, rare, bright features. The magnitude of such features depends on the scale observed, ranging from ~ 0.1 K for high resolution (0.25', 30 kHz), to few tens of mK for beams of size a few arcminutes. The peak magnitude is only weakly dependent on redshift, with the peak value within a factor of two of the typical values. The redshift/frequency at which the peak is reached is beamsize-dependent, moving to higher frequencies for larger beams. Taking also into account the much larger fluxes corresponding to larger beams, this again clearly argues for utilizing relatively large beams (5'-10' or more) and aiming at the high frequencies ($\sim 130 - 160$ MHz) for such observations. The statistics of such rare, bright peaks are also favourable at late times, we find that at $\sim 3' - 5'$ scales there are up to an order of magnitude more such peaks than a Gaussian statistics would predict.

4 KSZ EFFECT FROM PATCHY REIONIZATION

Next, we turn our attention to the second main reionization observable, the small-scale secondary CMB anisotropies generated through the kinetic Sunyaev-Zel'dovich (kSZ) effect (Zeldovich & Sunyaev 1969; Sunyaev & Zeldovich 1980; Ostriker & Vishniac 1986; Vishniac 1987; Jaffe & Kamionkowski 1998; Gruzinov & Hu 1998; Hu 2000; Gnedin & Jaffe 2001;

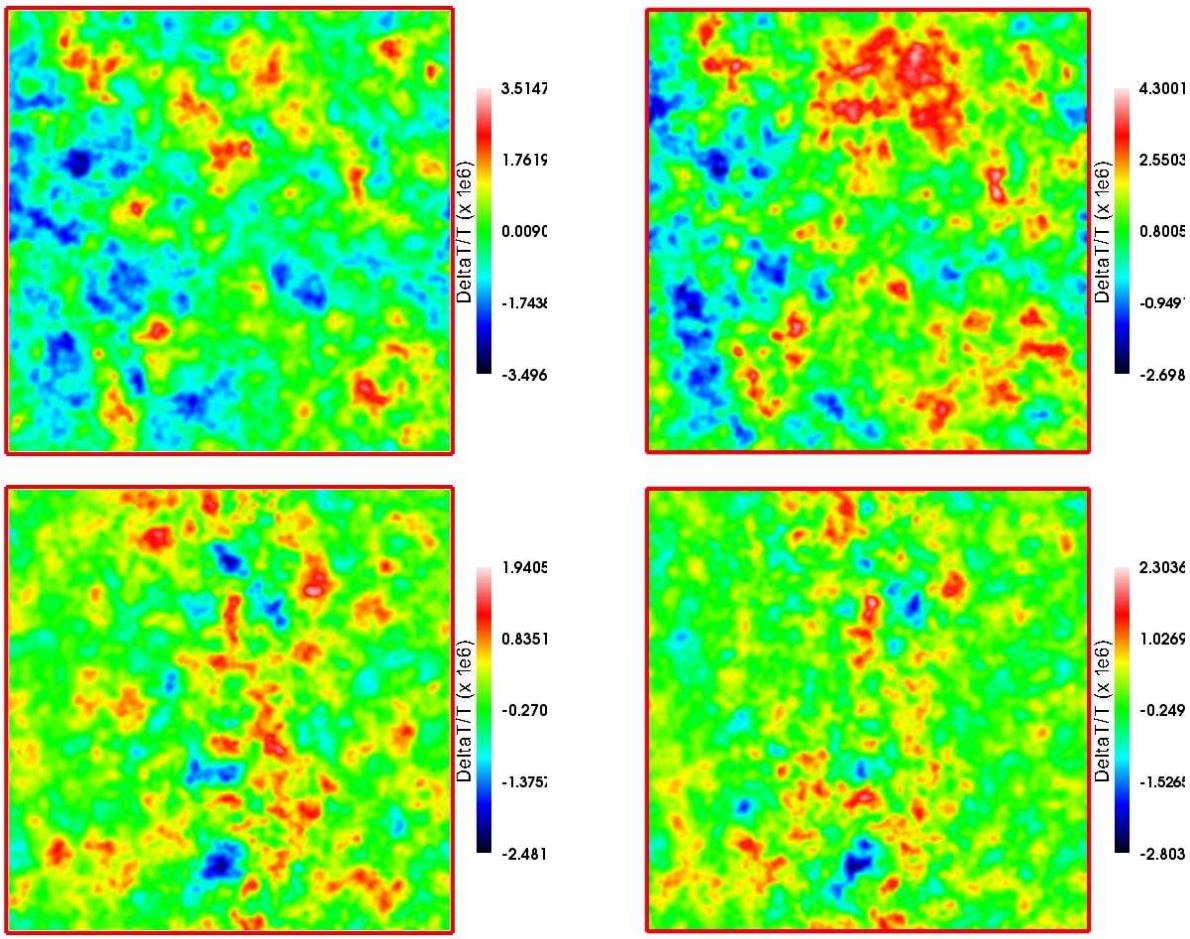

Figure 11. kSZ temperature fluctuation maps from simulations: f250 with large-scale velocities (top left), f250C with large-scale velocities (top right), f250 (bottom left), and f250C (bottom right). (Images produced using the Ifrit visualization package of N. Gnedin).

Springel et al. 2001; Ma & Fry 2002; Santos et al. 2003; Zhang et al. 2004; Zahn et al. 2005; McQuinn et al. 2005; Salvaterra et al. 2005; Iliev et al. 2006d). The kSZ effect results from Thomson scattering of the CMB photons onto electrons moving with a bulk velocity v. Along a line-of-sight (LOS) defined by a unit vector $\mathbf{n}$ the kSZ temperature anisotropies are given by:

$$\frac{\Delta T}{T_{\rm CMB}} = \int d\eta e^{-\tau_{\rm es}(\eta)} a n_e \sigma_T \frac{\mathbf{n}\cdot\mathbf{v}}{c}, \quad (5)$$

where $\eta = \int_0^t dt'/a(t')$ is the conformal time, a is the scale factor, $\sigma_T = 6.65 \times 10^{-25}\,{\rm cm}^{-2}$ is the Thomson scattering cross-section, and $\tau_{\rm es}$ is the corresponding optical depth. Since our simulation volume is not large enough to follow the complete photon light path from high redshift to the end of reionization, we have to combine several simulations volumes. In order to avoid artificial effects from the box repetition (in particular having the same structures repeating over and over along the photon path) we randomly shift the simulation box along both directions perpendicular to the ray direction and also alternate the x-, y- and z-directions of the box. We have presented our detailed methodology along with our predictions for the kSZ reionization signal based on WMAP1 cosmology in Iliev et al. (2006d). Some of the power from the largest-scale velocity field perturbations is missing from the simulation data, due to our finite box size. We compensate for that missing power by adding it in a statistical way, again as discussed in detail in Iliev et al. (2006d).

4.1 The kSZ signal

The resulting kSZ maps are shown in Figure 11. The full scale of the maps corresponds to our full simulation box size ($100\,h^{-1}$ Mpc, or $\sim 50'$) and the pixel resolution corresponds to the simulation cell size ($100\,h^{-1}/203\,{\rm Mpc} \approx 0.5\,{\rm h^{-1}Mpc}$, or $\sim 0.25'$). At a few arcminute scale there are a number of fluctuations larger than 5 μK with both positive and negative sign. The f250 and f250C runs yield largely similar level of fluctuations, slightly larger ones in the latter case. The typical scale of the kSZ temperature fluctuations in run f250 is also a bit larger than the scale for f250C, reflecting the larger, on average, sizes of the ionized regions in the former case compared to the latter. Introducing the correction for the missing large-scale velocity power increases the fluctuation range by about 50% and introduces some large-scale coherent motions.

In Figure 12 we show the PDF of these kSZ maps. The full range of the temperature fluctuations at pixel level is $\pm 20\,\mu$K ($\pm 13\,\mu$K) with (without) the large-scale velocity corrections. The *rms* fluctuations of $\Delta T/T_{\rm CMB}$ for run f250 are 4.835×10^{-7} (8.968×10^{-7}) without (with) large-scale velocities, while for run

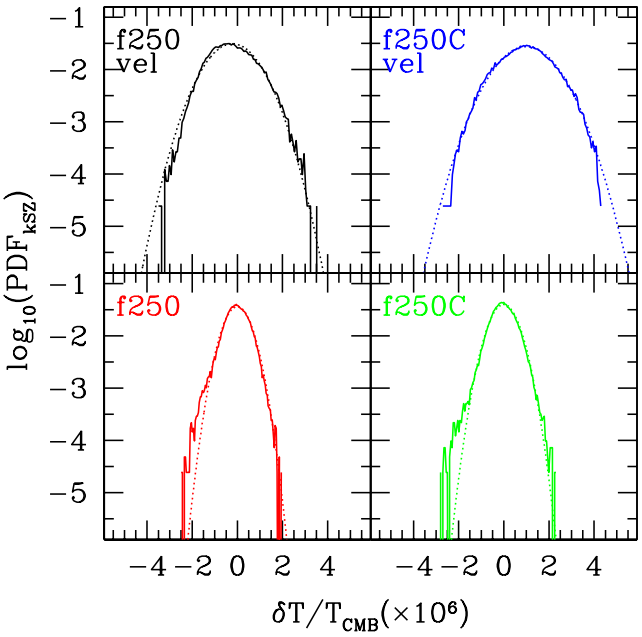

Figure 12. PDF distribution of $\delta T_{\rm kSZ}/T_{\rm CMB}$ (solid) vs. Gaussian distribution with the same mean and width (dotted) with (top panels) and without (bottom panels) correction for the large-scale velocity power missing from the computational box for our simulations, as labelled.

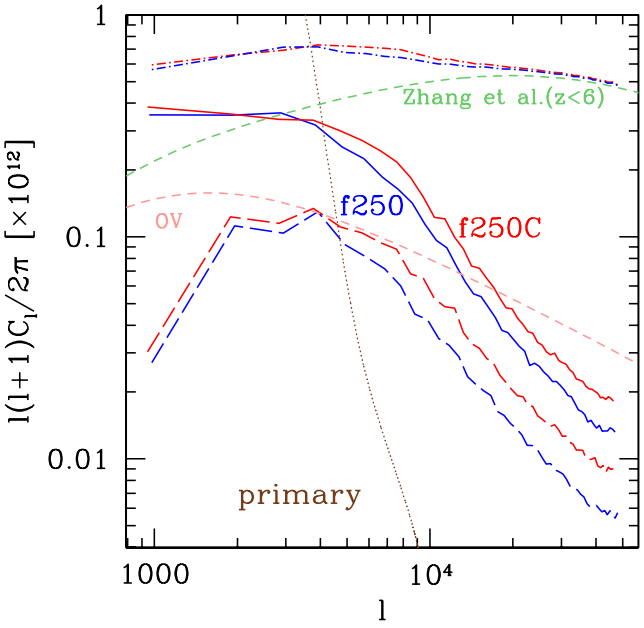

Figure 13. Sky power spectra of $\delta T_{\rm kSZ}/T_{\rm CMB}$ fluctuations resulting from our simulations: f250 (blue), and f250C (red). Solid (dashed) lines show the results with (without) the correction for the large-scale velocity power missing from the box. compared to the after-reionization kSZ signals (assuming overlap at $z_{\rm ov} = 8$): linear Ostriker-Vishniac effect, labelled 'OV' (long-dashed, pink), and a fully-nonlinear model matched to high-resolution hydrodynamic simulations of Zhang et al. (2004), labelled 'Zhang et al' (short-dashed, dark green). We also show the total (patchy reionization + Zhang et al. post-reionization) signals (dot-dashed; top lines) and the primary CMB anisotropy signal (dotted, brown).

f250C the numbers are 5.094×10^{-7} (1.020×10^{-6}) without (with) large-scale velocities. Both the range and the *rms* of the kSZ fluctuations are lower than the corresponding quantities we derived from the WMAP1 reionization scenarios by factor of ~ 2, thus the PDF distributions are correspondingly less wide. In both WMAP3 cases there are some mild departures from Gaussianity at the bright end. Adding the correction for the large-scale velocities yields wider (by factor of ~ 2) and very Gaussian PDF distributions.

Since the kSZ effect is a product of electron density and velocity, a naive expectation is that the kSZ angular power spectrum would scale as σ_8^2 for the density and σ_v^2 for the velocity, σ_8^4 in total. The actual ratio we find is $\sigma_8^{3.94}$ for reionization scenario f250C and $\sigma_8^{3.83}$ for f250. However since $8\,h^{-1}$Mpc is well above the scales relevant to reionization, thus in the presence of tilt a more appropriate scaling would be a bandpower at dwarf galaxy scales, $\sigma_{0.1}^2$, introduced in § 2, rather than at galaxy cluster scales, σ_8^2. We find the kSZ power scales as one power less, $\propto \sigma_{0.1}^{2.74}$ for f250C and $\propto \sigma_{0.1}^{2.82}$ for f250. This scaling also holds true for the minihalo bandpower, $\sigma_{0.01}^2$, hence becoming insensitive to the exact length scale once we are in the relevant part of the power spectrum. As we mentioned in § 1, the values of $\sigma_{0.01}$ and $\sigma_{0.1}$ scaled to include the growth inhibition between high redshift and redshift zero, $(a/D) \approx \Omega_m^{0.23}$, 0.74 and 0.76 for the WMAP3 and WMAP1 cases, provide a good indication when the hierarchy spanning the collapse of first the minihalos then the dwarfs developed.

The output from radio telescopes is sky power spectra, shown in Figure 13. The kSZ signal from patchy reionization dominates the primary anisotropy at small scales, for $\ell > 4000$. The magnitude of the signal is $[\ell(\ell+1)C_\ell/2\pi] \sim 10^{-13}$, or $\Delta T \sim 1\,\mu$K. The presence of sub-grid gas clumping boosts the power by $\sim 50\%$ for $\ell > 4000$, but has little effect on the power spectrum shape. Adding the correction for the missing velocity power at large-scales boosts the signal power by additional factor of 2-3 in the interesting range of scales ($\ell > 4000$). At larger scales the boost is larger, by up to an order of magnitude, but at those scales the kSZ temperature anisotropy is strongly dominated by the primary CMB. Compared to the predicted post-reionization anisotropy signals, the kSZ from patchy reionization is larger than the linear Ostriker-Vishniac signal (OV) for $\ell < 20,000$ and slightly lower than, but similar to the full nonlinear post-reionization effect prediction by Zhang et al. (2004) (which we rescaled to the current WMAP3 cosmology using the scaling $C_\ell \propto \sigma_8^5$). The total, patchy reionization and post-reionization (based on Zhang et al. (2004)) signals are also shown at the top of the figure. The total power spectrum retains the peak at $\ell \sim 3000 - 4000$ imprinted by the patchy reionization component, although the signal decrease at small scales is not as pronounced, since the decrease is partially compensated for by the continuing weak rise of the post-reionization component of the signal. The two reionization scenarios (red and blue top curves) would be very difficult to distinguish based solely on the total signal, but this might be possible to do if the post-reionization component is known sufficiently well and is subtracted to a good precision (see also the next section).

4.2 Observability: kSZ from patchy reionization

The Atacama Cosmology Telescope (Fowler 2004; Kosowsky & the ACT Collaboration 2006), which should be operational by March 2007, will observe at three frequency channels, 147, 215 and 279 GHz, targeting clear atmospheric windows,

with bandwidths 23, 23 and 32 GHz and at resolutions 1.7', 1.3' and 0.9', respectively. The target sensitivities in the three channels are 300, 500 and 700 $\mu\mathrm{K\,s}^{-1/2}$, respectively, with a final aim of $\sim 2\,\mu\,K$ per pixel over a large area of the sky ($\sim 200-400\,\mathrm{deg}^2$). The South Pole Telescope (SPT) (Ruhl & et al. 2006) will be observing in 5 frequency channels, 95, 150, 219, 274 and 345 GHz, with similar bandwidths and resolution to ACT. Its sensitivity could be even better, reaching $\sim 10\,\mu$K over 1 deg^2 in an hour. Thus, in terms of both resolution and sensitivity both telescopes are well-set to detect the patchy reionization kSZ signal.

The thermal noise of the detectors are given by

$$N_\ell = (sb)^2 \exp\left[\frac{\ell(\ell+1)b^2}{8\ln 2}\right] \quad (6)$$

assuming white noise with *rms* s and a Gaussian beam with FWHM of b. The error bar corresponding to a bin $\Delta\ell$ is then given by

$$(\Delta C_\ell)^2 = \frac{2}{(2\ell+1)\Delta\ell f_{\rm sky}}(C_\ell + N_{\ell,tot})^2, \quad (7)$$

where C_ℓ is our patchy reionization signal, $f_{\rm sky}$ is the sky coverage fraction of the survey and $N_{\ell,tot} = N_\ell + C_{\ell,primary} + C_{\ell,post-reion}$ is the average statistical noise for that bin. In the last expression we added the primary and post-reionization signals to the noise, since for the purposes of patchy power spectrum measurement we assume that the primary CMB fluctuations are well normalized, and can be statistically subtracted, contributing to the statistical noise. Similarly, the post-reionization kSZ signal was forecast robustly by Zhang et al. (2004) and would be subtracted from the power spectra, but contributes to the statistical errors. In Figure 14 we show our predicted kSZ signal for both of our WMAP3 reionization models along with the ACT (left) and SPT (right) expected sensitivities, for $s = 3.3\,\mu K$, $b = 1.1'$, 100 deg^2 area (ACT; $f_{\rm sky} = 100/41253 = 0.0024$; Huffenberger & Seljak (2005)) and $s = 11.5\,\mu K$, $b = 1'$, 4000 deg^2 area (SPT; $f_{\rm sky} = 4000/41253 = 0.097$). This assumes perfect subtraction of all other foregrounds. Results show that the reionization signal should be observable with both ACT and SPT and in principle could even distinguish different reionization scenarios. A number of difficult questions remain to be answered, however.

The detected signal would be a mixture of thermal Sunyaev-Zel'dovich (tSZ) from galaxy clusters, gravitational lensing-induced anisotropies, Galactic dust and extragalactic point sources (e.g. dust in high redshift galaxies), in addition to the kSZ patchy reionization and post-reionization components. Separating these signals from each other presents significant challenges. The tSZ signal, which tends to dominate at these frequencies could be separated through its characteristic spectral shape, and in particular using the fact that the signal goes to zero at 217 GHz in the Earth frame. Detecting the galaxy clusters with tSZ could allow the derivation and subtraction of their kSZ contribution, as well, through detailed modelling of the clusters based on their tSZ data. The bright point sources could be subtracted based on complementary observations with e.g. ALMA. The lensing contribution is spectrally the same as the kSZ signal (and the same as the primary CMB anisotropies), but is statistically-different from the kSZ, which should allow their separation, at least in principle (Riquelme & Spergel 2006).

The most difficult problem is to separate the patchy reionization and the post-reionization kSZ signals since both their spectra and their statistics are the same. Such separation is required, however if we want to extract any reionization information from the detected kSZ signal. This could be done for example by sufficiently detailed modelling of the post-reionization signal and its properties. The linear effect, also called Ostriker-Vishniac (OV) effect, can now be calculated with a reasonable precision, but it significantly underestimates the actual post-reionization signal. The full nonlinear kSZ post-reionization effect is still difficult to derive from simulations due to insufficient dynamic range. Current models and simulations roughly agree, but only within a factor of 2 at best, which would not allow for precise enough subtraction. Another option is to use the characteristic, fairly sharp peak of the patchy signal at ℓ of a few thousand, which is in contrast to the much broader peak of the post-reionization signal.

5 CONCLUSIONS

We presented detailed predictions of the signatures of inhomogeneous reionization at redshifted 21-cm line of hydrogen and kSZ-induced CMB small-scale anisotropies. Our results are based on the largest-scale radiative transfer simulations to date, utilizing a background cosmology given by the WMAP 3-year data. In combination with our previously-presented similar results based on the WMAP1 cosmology they bracket the range of variation of these reionization observables due to uncertainties in the overall density power spectrum normalization.

Not surprisingly, the amplitude change has a significant effect on the reionization observables, even without changing any of the "astrophysical control parameters" such as source efficiencies and escape fractions. The lower normalization of the power spectrum of density fluctuations (lower σ_8), its tilt $n_s < 1$, and the lower matter density, Ω_m all work to delay the formation of cosmological structures, and even more so at small scales because of the tilt. Assuming the same ionizing photon emissivities per atom, this delay in the structure formation naturally leads to a corresponding delay of reionization. Many of the basic features of the reionization process and its signatures remain largely the same, however. This includes e.g. the typical sizes of the ionized and neutral patches, the levels of the 21-cm *rms* fluctuations and the bright individual features and their statistics. Such offset to later times would move the redshifted 21-cm signals to higher frequencies. This would make them easier to detect since the foregrounds decrease with increasing frequency, by factor up to a few, while at the same time the detector sensitivities improve. Furthermore, late reionization scenarios yield peak values of the 21-cm fluctuation signals which are farther from the FM bands (90-110 MHz) than do the early-reionization scenarios. This is very important for some experiments, like LOFAR, which are located in high-RFI environments.

In contrast, the kSZ CMB anisotropy signal due to patchy reionization decreases for late-reionization models by factor of a few when compared to early-reionization scenarios. The origin of the kSZ signal is relatively complicated, since it is an integrated signal over the entire epoch of reionization, and depends on the gas density, velocity and ionized fraction. At corresponding stages of structure formation and reionization the overdensities (the cosmic web), bulk velocities and ionization level and patchiness are all similar in the two types of scenarios. However, the mean gas density at the corresponding times is lower for the late-reionization models, resulting in a lower amplitude of the signal. We find the *rms* of the kSZ signal from patchy reionization scales as $\sim \sigma_{0.1}^3$, where $\sigma_{0.1}$ is the *rms* density fluctuations extrapolated to the present on the dwarf galaxy scale of $0.1h^{-1}\mathrm{Mpc}$ according to the linear perturbation theory. The other properties of the kSZ signal are similar between the two cosmologies, e.g. its shape,

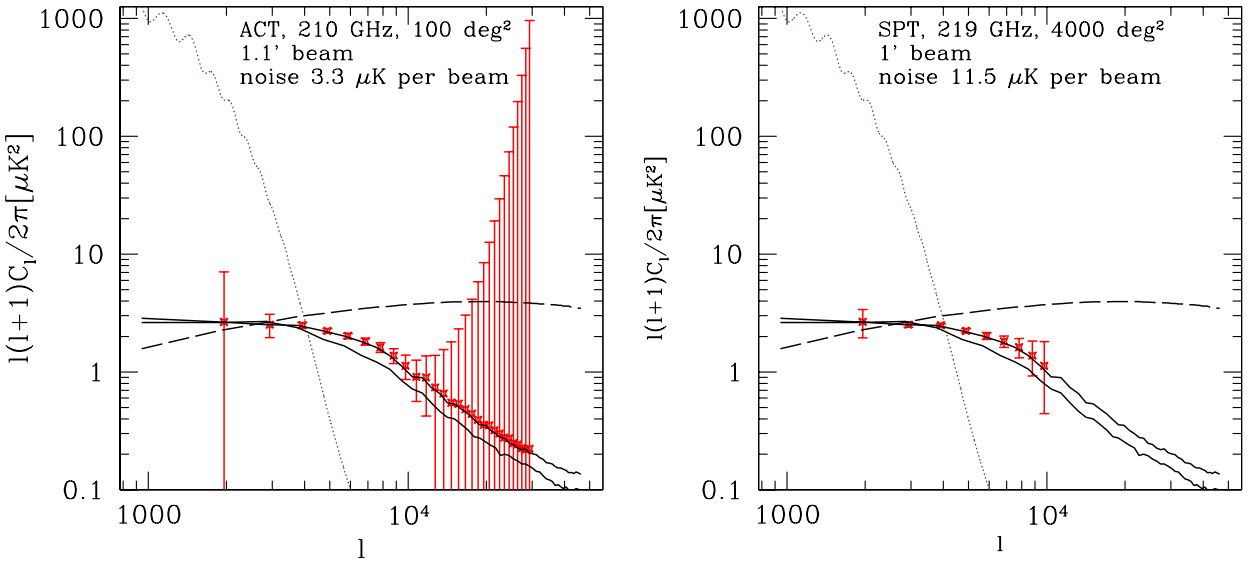

Figure 14. Observability of the kSZ: the sky power spectrum of the reionization signal (black, solid; simulations f250 and f250C) with the forecast error bars for ACT (left) and SPT (right) vs. ℓ. The primary CMB anisotropy (dotted) and the post-reionization kSZ signal (dashed) are also shown and are added to the noise error bars for the reionization signal. Cosmic variance from tSZ would increase the error bars, but here we are assuming that the tSZ component has been completely separated, by virtue of its characteristic spectral shape.

which has a clear peak at $\ell \sim 3000 - 4000$ and a strong decline at small scales, $\ell > 10^4$. The patchy kSZ signal around the peak is of comparable magnitude to the estimated post-reionization CMB anisotropy component (which also decreases for WMAP3 parameters compared to WMAP1, roughly as σ_8^5).

We discussed the observability of these signals in view of the expected parameters and sensitivities of current and upcoming 21-cm and kSZ experiments. We suggested some observational strategies based on our results. In particular, the best approach for detecting the redshifted 21-cm observations is to utilize relatively large beam sizes (a few arcminutes or more) and bandwidths (hundreds of kHz), which would result in large gains in flux, while retaining most of the signal. Additionally, it is better to concentrate on the high frequencies, above 120 MHz, since the 21-cm fluctuations, the corresponding fluxes and instrument sensitivities peak there, while the foregrounds are noticeably lower than they are at lower frequencies.

An important caveat is that the results presented in this work are based on reionization simulations which do not resolve the smallest atomically-cooling halos, with masses from $\sim 10^8$ to $\sim 2{\times}10^9\ M_\odot$ and the even smaller molecularly-cooling minihalos. Smaller-box, higher-resolution radiative transfer simulations which included all atomically-cooling halos (Iliev et al. 2006c) showed that the presence of low-mass sources results in self-regulation of the reionization process, whereby $\tau_{\rm es}$ is boosted, while the large-scale structure of reionization and the epoch of overlap are largely unaffected. This is a consequence of the strong suppression of these low-mass sources due to Jeans-mass filtering in the ionized regions. We expect that this self-regulation would not affect our current results significantly since the reionization signals discussed in this work are dominated by the large bubbles. Utilizing smaller computational boxes in order to resolve the low-mass sources makes the problem more manageable, but results would underestimate the large-scale power of the ionization fluctuations and be subject to a large cosmic variance. Resolving all halos of mass $\sim 10^8 M_\odot$ or larger in $100\,h^{-1}$ Mpc box would require $\sim 10^{11}$ particles, with the additional complication that on such small scales gasdynamical effects also become important and thus the complete treatment would require a fully self-consistent N-body, gasdynamics and radiative transfer. While still quite difficult, such simulations are now becoming possible with the available algorithms and computer hardware. Future higher-resolution calculations with more detailed microphysics would allow us to evaluate more stringently the effects of low-mass sources and small-scale structure on the reionization observables.

ACKNOWLEDGMENTS

We thank Wayne Hu and and Arthur Kosowsky for supplying the sensitivity data for SPT and ACT, respectively and for useful discussions. This work was partially supported by NASA Astrophysical Theory Program grants NAG5-10825 and NNG04G177G to PRS.

REFERENCES

Alvarez M. A., Shapiro P. R., Ahn K., Iliev I. T., 2006, ApJL, 644, L101

Chuzhoy L., Alvarez M. A., Shapiro P. R., 2006, ApJL, 648, L1

Dore O., Holder G., Alvarez M., Iliev I. T., Mellema G., Pen U.-L., Shapiro P. R., 2007, ArXiv Astrophysics e-prints

Field G. B., 1959, ApJ, 129, 536

Fowler J. W., 2004, in Z-Spec: a broadband millimeter-wave grating spectrometer: design, construction, and first cryogenic measurements. Edited by Bradford, C. Matt; Ade, Peter A. R.;

Aguirre, James E.; Bock, James J.; Dragovan, Mark; Duband, Lionel; Earle, Lieko; Glenn, Jason; Matsuhara, Hideo; Naylor, Bret J.; Nguyen, Hien T.; Yun, Minhee; Zmuidzinas, Jonas. Proceedings of the SPIE, Volume 5498, pp. 1-10 (2004)., Bradford C. M., Ade P. A. R., Aguirre J. E., Bock J. J., Dragovan M., Duband L., Earle L., Glenn J., Matsuhara H., Naylor B. J., Nguyen H. T., Yun M., Zmuidzinas J., eds., pp. 1–10

Furlanetto S. R., Loeb A., 2002, ApJ, 579, 1

—, 2004, ApJ, 611, 642

Furlanetto S. R., Oh S. P., Briggs F. H., 2006, Physics Reports, 433, 181

Gnedin N. Y., Jaffe A. H., 2001, ApJ, 551, 3

Gruzinov A., Hu W., 1998, ApJ, 508, 435

Holder G., Iliev I. T., Mellema G., 2006, ArXiv Astrophysics e-prints (astro-ph/0609689)

Hu W., 2000, ApJ, 529, 12

Huffenberger K. M., Seljak U., 2005, New Astronomy, 10, 491

Iliev I. T., Ciardi B., Alvarez M. A., Maselli A., Ferrara A., Gnedin N. Y., Mellema G., Nakamoto T., Norman M. L., Razoumov A. O., Rijkhorst E.-J., Ritzerveld J., Shapiro P. R., Susa H., Umemura M., Whalen D. J., 2006a, MNRAS, 371, 1057

Iliev I. T., Mellema G., Pen U.-L., Merz H., Shapiro P. R., Alvarez M. A., 2006b, MNRAS, 369, 1625

Iliev I. T., Mellema G., Shapiro P. R., Pen U. L., 2006c, MNRAS, in press (astro-ph/0607517)

Iliev I. T., Pen U.-L., Bond J. R., Mellema G., Shapiro P. R., 2006d, ApJ, submitted, ArXiv Astrophysics e-prints (astro-ph/0609592)

Iliev I. T., Pen U.-L., Richard Bond J., Mellema G., Shapiro P. R., 2006e, New Astronomy Review, 50, 909

Iliev I. T., Scannapieco E., Martel H., Shapiro P. R., 2003, MNRAS, 341, 81

Iliev I. T., Shapiro P. R., Ferrara A., Martel H., 2002, ApJL, 572, L123

Jaffe A. H., Kamionkowski M., 1998, Phys. Rev. D, 58, 043001

Kosowsky A., the ACT Collaboration, 2006, ArXiv Astrophysics e-prints (astro-ph/0608549)

Kuo C. L., et al., 2006, ApJ, submitted (astro-ph/0611198)

Ma C.-P., Fry J. N., 2002, Physical Review Letters, 88, 211301

McQuinn M., Furlanetto S. R., Hernquist L., Zahn O., Zaldarriaga M., 2005, ApJ, 630, 643

Mellema G., Iliev I. T., Alvarez M. A., Shapiro P. R., 2006a, New Astronomy, 11, 374

Mellema G., Iliev I. T., Pen U.-L., Shapiro P. R., 2006b, MNRAS, 372, 679

Merz H., Pen U.-L., Trac H., 2005, New Astronomy, 10, 393

Ostriker J. P., Vishniac E. T., 1986, ApJL, 306, L51

Pritchard J. R., Furlanetto S. R., 2006, ArXiv Astrophysics e-prints (astro-ph/0607234)

Riquelme M. A., Spergel D. N., 2006, ArXiv Astrophysics e-prints (astro-ph/0610007)

Ruhl J. E., et al., 2006, Proc. SPIE, 5498, 11

Salvaterra R., Ciardi B., Ferrara A., Baccigalupi C., 2005, MNRAS, 360, 1063

Santos M. G., Cooray A., Haiman Z., Knox L., Ma C.-P., 2003, ApJ, 598, 756

Seljak U., Slosar A., McDonald P., 2006, ArXiv Astrophysics e-prints (astro-ph/0604335)

Shapiro P. R., Ahn K., Alvarez M. A., Iliev I. T., Martel H., Ryu D., 2006, ApJ, 646, 681

Shaver P. A., Windhorst R. A., Madau P., de Bruyn A. G., 1999, *A.&A*, 345, 380

Spergel D. N., et al., 2006, ArXiv Astrophysics e-prints (arXiv:astro-ph/0603449)

Spergel D. N., Verde L., Peiris H. V., Komatsu E., Nolta M. R., Bennett C. L., Halpern M., Hinshaw G., Jarosik N., Kogut A., Limon M., Meyer S. S., Page L., Tucker G. S., Weiland J. L., Wollack E., Wright E. L., 2003, ApJS, 148, 175

Springel V., White M., Hernquist L., 2001, ApJ, 549, 681

Sunyaev R. A., Zeldovich I. B., 1980, MNRAS, 190, 413

Vishniac E. T., 1987, ApJ, 322, 597

Yao W.-M., et al., 2006, Journal of Physics G Nuclear Physics, 33, 1

Zahn O., Zaldarriaga M., Hernquist L., McQuinn M., 2005, ApJ, 630, 657

Zeldovich Y. B., Sunyaev R. A., 1969, Ap&SS, 4, 301

Zhang P., Pen U.-L., Trac H., 2004, MNRAS, 347, 1224